remote sensing

MDPI

Article

Estimation of Particulate Organic Carbon Concentration and Its Driving Factors in Lakes of the Yangtze–Huaihe Plain, China

Pengyao Cao [1], Xinchang Zhang [1], Hengkai Li [2], Shuai Zeng [3], Shaohua Lei [4], Ge Liu [5] and Yongjian Ruan [1,*]

[1] School of Geography and Remote Sensing, Guangzhou University, Guangzhou 510006, China; 2112401056@e.gzhu.edu.cn (P.C.); zhangxc@gzhu.edu.cn (X.Z.)
[2] Jiangxi Provincial Key Laboratory of Water Ecological Conservation in Headwater Regions, Jiangxi University of Science and Technology, 1958 Ke-Jia Road, Ganzhou 341000, China; giskai@jxust.edu.cn
[3] South China Institute of Environmental Science, Ministry of Ecology and Environment, No. 18 Ruihe Rd., Guangzhou 510535, China; szeng@scies.org
[4] National Key Laboratory of Water Disaster Prevention, Nanjing Hydraulic Research Institute, Nanjing 210029, China; shaohualei@nhri.cn
[5] Northeast Institute of Geography and Agroecology, Chinese Academy of Sciences, Shengbei Street No. 4888, Changchun 130102, China; liuge@iga.ac.cn
* Correspondence: ruanyj@gzhu.edu.cn

Highlights

What are the main findings?

- A semi-analytical algorithm was developed to estimate particulate organic carbon concentrations in inland waters using Sentinel-2 MSI data.
- Its application revealed spatial and temporal patterns across 90 Yangtze–Huaihe Plain lakes during 2018–2024, with concentrations associated with chlorophyll-a, total phosphorus, and meteorological and catchment indicators.

What are the implications of the main findings?

- The approach supports regional assessment of lake particulate organic carbon patterns and their environmental associations.
- Further independent satellite validation and uncertainty assessment are needed before operational use in lake management and carbon accounting.

Abstract

Inland lake ecosystems function as active nodes in the global carbon cycle, yet reliable basin-scale estimates of particulate organic carbon concentration (C_{POC}) remain scarce owing to the optical complexity of these environments. In this study, POC denotes the total particulate organic carbon pool, including organic matter from living and non-living particles. Here we present a semi-analytical retrieval scheme tailored to Sentinel-2 Multispectral Instrument (MSI) data and applied to 90 large eutrophic lakes (each >10 km^2) within the Yangtze–Huaihe Plain (YHP) of eastern China. The scheme reconstructs the particulate absorption coefficient at 665 nm, $a_p(665)$, from reflectance measurements at 665, 705, and 740 nm, reducing the interference of colored dissolved organic matter (a_{CDOM}) absorption and particulate backscattering (b_b). When evaluated against 60 field observations in the predefined concentration-stratified holdout, the algorithm achieved MAE = 0.59 mg/L, RMSE = 0.73 mg/L, and MAPE = 46.89%—outperforming three widely cited benchmark algorithms—and showed preliminary transfer potential in the two estuarine datasets. MSI-derived C_{POC} maps from 2018 to 2024 revealed systematic east-to-west and center-to-periphery concentration gradients across the 90-lake assemblage, shaped by catchment nutrient delivery, basin hydrodynamics, and phytoplankton standing stock. Correlation and

Check for updates

Academic Editor: Gabriel Senay

Received: 11 September 2026
Revised: 23 October 2026
Accepted: 31 October 2026
Published: 6 November 2026

Copyright: © 2026 by the authors. Licensee MDPI, Basel, Switzerland. This article is an open access article distributed under the terms and conditions of the Creative Commons Attribution (CC BY) license.

attribution analyses identified chlorophyll-a concentration (C_{Chla}), atmospheric pressure, and total phosphorus (C_{TP}) as the three dominant environmental modulators of C_{POC} variability. The framework provides a field-calibrated approach for examining regional lake C_{POC} patterns. Its satellite application and ability to distinguish small concentration differences require further independent validation and uncertainty assessment.

Keywords: particulate organic carbon; semi-analytical algorithm; Sentinel-2 MSI; Yangtze–Huaihe Plain; eutrophication

1. Introduction

Carbon bound to suspended organic particles—collectively termed particulate organic carbon (POC)—occupies a central position in the material and energy economy of aquatic ecosystems [1,2]. As the principal substrate of the biological pump, sinking POC transfers photosynthetically fixed carbon from the sunlit surface layer to depth, effectively sequestering it from the atmosphere on timescales ranging from decades to millennia [3,4]. At the sediment interface, POC sustains benthic microbial communities and drives nutrient remineralization, with cascading consequences for oxygen dynamics and the availability of dissolved nutrients in the water column [5–7]. Monitoring C_{POC} is therefore essential not only for constraining inland-water carbon budgets but also for evaluating lake ecological status and water-quality dynamics [8–10]. Despite its ecological and biogeochemical importance, obtaining spatially continuous observations of C_{POC} remains challenging.

Traditional approaches to C_{POC} quantification—filtration, combustion, and spectrophotometric analysis of discrete water samples—generate high-quality point data but are poorly suited to capturing the spatial heterogeneity and temporal dynamics of large lake networks [2,11–13]. Satellite remote sensing circumvents these limitations by delivering synoptic, time-series observations at manageable cost [14–16]. Three algorithmic paradigms have been pursued to translate satellite-measured reflectance R_{rs} into C_{POC} estimates [9,17–20]. Empirical regression models (Type I) exploit statistical covariance between R_{rs} band combinations and in-situ C_{POC}; they are straightforward to implement but tend to be regionally specific and deteriorate in optically complex waters where multiple constituents covary [1,9,21]. Chlorophyll-a-mediated approaches (Type II) first retrieve C_{Chla} and then invoke an empirically established C_{Chla}–C_{POC} relationship; this strategy performs acceptably in phytoplankton-dominated open-ocean settings [16,19,22–24] but breaks down wherever non-algal particles or terrestrial organic matter decouple the two variables—a situation documented [7,11], for instance, in the Pearl River Estuary where the C_{POC}–C_{Chla} correlation fell below r = 0.5 [25]. Semi-analytical models (Type III) invert inherent optical properties (IOPs) through radiative-transfer theory, offering greater mechanistic fidelity and broader transferability, yet they still require system-specific optical parameterization and iterative optimization [7,19,22]. Developing an algorithm that combines the interpretability of Type III with the operational simplicity of Type I therefore remains an active research frontier.

The YHP—spanning the middle–lower reaches of the Yangtze River Basin (YRB) and the Huai River Basin (HRB) in eastern China—presents an ideal yet underexplored test bed for regional C_{POC} monitoring [26,27]. Decades of intensifying agriculture, urban expansion, and hydrological modification have pushed more than 85% of YHP lakes into eutrophic or hypereutrophic states [28,29], substantially altering their carbon storage and export dynamics. Previous remote-sensing studies have concentrated on a small number of large, turbid flagship lakes such as Lake Taihu and Lake Chaohu, leaving the broader lake network—particularly small-and medium-sized water bodies—without adequate coverage [1,7,21]. Sentinel-2 MSI, with its 10–20 m spatial resolution and enhanced signal-to-noise

ratio (SNR) [30,31], is uniquely positioned to bridge this gap: it resolves intra-lake spatial structure that coarser ocean-color sensors such as MODIS and MERIS cannot, while its five-day revisit cycle enables near-continuous temporal monitoring [32,33]. Nevertheless, regional-scale C_{POC} retrieval based on Sentinel-2 MSI across heterogeneous lake systems remains scarce, and its applicability beyond several well-studied eutrophic lakes has not been systematically evaluated.

The retrieval model was developed and validated using field observations from nine representative lakes (180 samples) and was subsequently applied to 90 large eutrophic lakes across the Yangtze–Huaihe Plain. Motivated by the above considerations, this study develops an MSI-compatible semi-analytical C_{POC} algorithm, deploys it across 90 YHP lakes over a seven-year period (2018–2024), and examines environmental associations with the observed C_{POC} variability. Three specific questions guide the analysis: (1) Can a physically interpretable, MSI-based C_{POC} scheme provide useful prediction within the sampled lakes and for previously unseen lakes? (2) What spatiotemporal patterns characterize C_{POC} distribution across this diverse lake assemblage? (3) Which environmental and anthropogenic factors are most strongly associated with C_{POC} dynamics in the YHP?

2. Study Area

Situated in the East Asian monsoon zone, the YHP encompasses a dense mosaic of interconnected lakes that collectively underpin regional freshwater supply, flood attenuation, and biodiversity conservation [34,35]. Progressive anthropogenic pressures—agricultural intensification, industrial expansion, and widespread land-cover conversion—have reshaped the hydrological connectivity of the region over recent decades, compressing lake areas and accelerating nutrient accumulation [28,36–38].

This study focuses on 90 eutrophic lakes with individual surface areas exceeding 10 km^2, comprising 72 lakes in the middle–lower YRB and 18 in the HRB. River channels, canals, and smaller water bodies were excluded to concentrate exclusively on lacustrine systems. Lake surface areas span three orders of magnitude (10–3583 km^2), capturing a broad range of morphometric, trophic, and catchment conditions [39,40]. This diversity provides a demanding and ecologically representative testing ground for algorithm development and cross-system comparison [41]. The selected lakes collectively encompass the major trophic and hydrological gradients present across the YHP, thereby facilitating the development of a regionally representative retrieval model. The nine field-sampled lakes used for algorithm development and evaluation are included in this 90-lake regional application set; their names also appear in Table S4.

3. Data and Methods

The study follows four stages: algorithm development and evaluation using field observations from nine lakes; transfer testing in two independent estuarine datasets; comparison with three published algorithms; and satellite application to the 90-lake regional set. The nine field-sampled lakes are included in the regional application set. Driving-factor analyses follow the regional application and retain their distinct field-observation and lake–year data scopes.

3.1. Algorithm Development and Evaluation Using Nine Lakes

3.1.1. Field Observations and Dataset Partitioning

Between 2017 and 2020, nine field campaigns were conducted across the YHP, yielding 180 water samples together with concurrent in-situ Rrs measurements (Figure 1). Sampling campaigns covered nine representative lakes across the YHP, including Lake Poyang, Lake Dongting, Lake Taihu, Lake Hongze, Lake Chaohu, Lake Gaoyou, Lake Shijiu, Lake Nanyi,

and Lake Gehu (Table 1). Sampling took place during 2017–2020; the number of samples collected from each lake is reported in Table 1. At each station, one-liter surface-water aliquots were collected and stored in amber bottles at 4 °C until laboratory analysis concentrations of total nitrogen (C_{TN}), total phosphorus (C_{TP}), total suspended matter (C_{TSM}), C_{POC}, C_{Chla}, and water clarity (SDD).

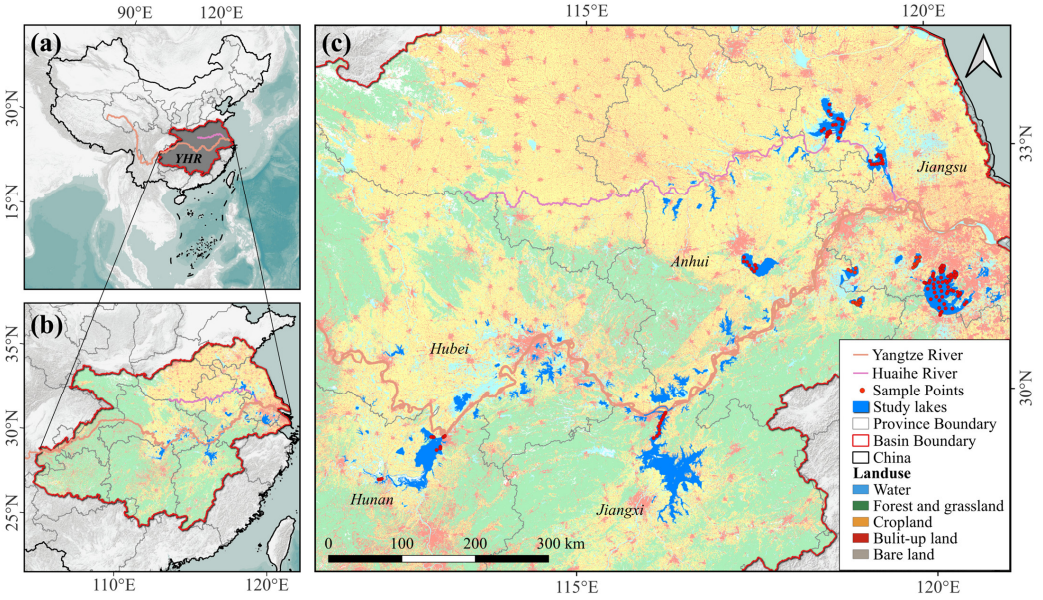


Figure 1. Spatial distribution of the study area and sampling points. (**a**) Location of the Yangtze–Huaihe River (YHR) basin in China; (**b**) Distribution of study lakes within the YHR basin; (**c**) Detailed land use patterns, sample points, and study lakes in the specific study area.

Table 1. The general geographical information (name, location, water area (in km^2), and sampling number (SN)) of 9 sampling lakes, and the collected monthly mean meteorological data (wind speed (WP, in m/s), air temperature (Tem, in °C), precipitation (Pre, in mm), and mean particulate organic carbon concentration (C_{POC}, in mg/L)) between 2018 and 2024 are listed.

Code	Lake	Lon.	Lat.	Area	SN	WS	Tem	Pre	Mean POC
L1	Poyang	116.23	29.19	3150	16	1.67	19.12	147	2.56
L2	Dongting	112.7	29.3	2625	20	2.04	17.2	140	1.85
L3	Taihu	120.16	31.23	2574	60	1.72	16.4	98.03	7.62
L4	Hongze	118.71	33.3	2069	30	2.08	15.99	91.4	1.76
L5	Chaohu	117.56	31.52	780	18	2.26	16.77	101.5	7.74
L6	Gaoyou	119.32	32.83	760.6	14	2.01	15.32	86.4	3.58
L7	Nanyi	118.97	31.1	205.1	6	1.95	16.4	102.4	1.31
L8	Gehu	119.81	31.6	139.5	9	1.91	16.05	107.8	4.05
L9	Shijiu	118.88	31.48	222.1	7	2.03	16.4	104.4	5.05

Remote sensing reflectance data were acquired using an ASD spectroradiometer (350–2390 nm), following the standard above-water radiometric protocols recommended by Mueller et al. [42]. To minimize sun-glint contamination, the viewing geometry was 135° in azimuth relative to the Sun and 40° from nadir, as recommended by Mobley [43]. At each station, triplicate measurements of water-viewing total radiance (L_t), sky radiance (L_{sky}), and reference-panel radiance (L_p) were recorded, each averaged over 10 consecutive scans to improve the signal-to-noise ratio (SNR). R_{rs} was calculated as follows:

$$R_{rs}(\lambda) = \frac{L_t - r \cdot L_{sky}}{\pi \cdot \left(L_p / \rho_p\right)} \quad (1)$$

Here, L_t is the total radiance measured in the water-viewing direction before sky-reflection correction; L_{sky} and L_p are the measured sky and reference-panel radiances, respectively; r is the air–water interface reflectance coefficient; and ρ_p is the certified reflectance of the Spectralon® reference panel (Labsphere, Inc., North Sutton, NH, USA). HydroLight calculations provide a basis for estimating r under the relevant illumination and viewing conditions [43]. R_{rs} is expressed in sr^{-1}.

To characterize the optical diversity, the in-situ R_{rs} spectra were truncated to the common 400–760 nm range across all lakes, and a lake-specific median spectrum was subsequently derived from all measurements at each wavelength (Figure S10).

The full dataset from the nine field-sampled lakes (N = 180) was stratified by ascending C_{POC} and partitioned using a one-in-three systematic rule: every third sample was assigned to the concentration-stratified holdout subset (N = 60), and the remaining two-thirds constituted the calibration subset (N = 120). To further diagnose whether the holdout split inadvertently retained spatial dependency, a lake-wise leave-one-lake-out (LOLO) cross-validation was performed. In each LOLO fold, all samples from a single lake were withheld for testing, while the empirical POC relationship was recalibrated using the remaining lakes. Notably, this LOLO procedure does not ensure temporal independence due to repeated sampling within the same lake over time; it was therefore treated solely as a transferability diagnostic rather than a replacement for the predefined 120/60 calibration-holdout evaluation.

3.1.2. Laboratory and Optical Measurements

Standard analytical procedures were applied throughout. C_{TN} and C_{TP} were quantified following established colorimetric methods [44,45]; C_{Chla} was extracted with ethanol and measured spectrophotometrically [46,47]. For C_{POC}, water was filtered through pre-combusted quartz-fiber filters (450 °C, 6 h), subjected to vapor-phase HCl acidification (concentrated HCl, 12 h) to eliminate inorganic carbon, dried at 60 °C for 48 h, and combusted at 1080 °C in an Elementar vario TOC cube analyzer (Elementar Analysensysteme GmbH, Langenselbold, Germany).

Spectral inherent optical properties (IOPs) were characterized in parallel. CDOM absorption ($(a_{CDOM}$) was determined spectrophotometrically using filtered (0.2 µm) water samples. Total particulate absorption (a_p) was derived via the quantitative filter technique (QFT) with path-length amplification correction [48,49]. Non-algal particulate absorption (a_{nap}) was isolated after bleaching with 10% sodium hypochlorite (20 min) [50], and phytoplankton absorption (a_{ph}) was calculated as

$$a_{ph}(\lambda) = a_p(\lambda) - a_{nap}(\lambda) \quad (2)$$

across 400–750 nm using a dual-beam spectrophotometer with an integrating sphere.

3.1.3. Semi-Analytical Algorithm Construction

Considering the band settings of Sentinel-2 MSI data used in this study, the particulate absorption coefficient (a_p) at 665 nm was selected as a physically relevant intermediate optical indicator of C_{POC} because it showed the strongest association among the examined particulate absorption variables (r = 0.68; Figure S1a). The main idea of the proposed algorithm was to construct a remote sensing reflectance index strongly related to a_p from $R_{rs}(665)$, $R_{rs}(705)$, and $R_{rs}(740)$ of Sentinel-2 MSI, and further derive C_{POC} based on its empirical relationship with the latter. The descriptions and corresponding abbreviations are shown in Table 2. This relationship motivates the three-band optical formulation developed below; the predictive performance of the complete retrieval scheme is assessed independently in Section 4.1.

Table 2. Abbreviations, principal symbols, and units used in this study.

Symbol	Description	Unit
YRB	Yangtze River Basin	
HRB	Huai River Basin	
YHP	Yangtze–Huaihe Plain	
POC	Particulate organic carbon	—
Chla	Chlorophyll-a	ug/L
SDD	Water clarity	m
TSM	Total suspended matter	mg/L
TN	Total nitrogen	mg/L
TP	Total phosphorus	mg/L
L_t	Water-leaving radiance	
L_{sky}	Sky radiance	
L_p	Reference panel radiance	
SNR	Signal-to-noise ratio	
DSF	Dark spectrum fitting	
VB-FAH	Virtual-Baseline Floating macroAlgae Height	
Lon.	Longitude	
Lat.	Latitude	
SN	Sampling number	
WS	Wind speed (m/s)	m/s
Tem	Air temperature (°C)	°C
Pre	Precipitation (mm)	mm
λ	Wavelength	nm
$R_{rs}(\lambda)$	Remote sensing reflectance at λ	sr^{-1}
$a(\lambda)$	Total absorption coefficients at λ	m^{-1}
$a_p(\lambda)$	Absorption coefficients of particle matter at λ	m^{-1}
$b_b(\lambda)$	Backscattering coefficient of water components	m^{-1}
$a_{CDOM}(\lambda)$	Absorption coefficients of CDOM at λ	m^{-1}
$a_{ph}(\lambda)$	Absorption coefficients of phytoplankton pigment at λ	m^{-1}
$a_{nap}(\lambda)$	Absorption coefficients of non-algal particle at λ	m^{-1}
$a_{nw}(\lambda)$	Absorption coefficients of non-water components at λ	m^{-1}
$a_w(\lambda)$	Absorption coefficients of pure water at λ	m^{-1}
MAE	Mean Absolute Error	mg/L
MAPE	Mean absolute percentage difference	%
RMSE	Root mean square error	mg/L
R^2	Predictive coefficient of determination for evaluation records	—
C_{POC}	Particulate organic carbon concentration	mg/L
ρ_p	Certified reflectance of the reference panel	—
r	Air–water interface reflectance coefficient in the radiometric correction	—
N	Number of paired observations in the stated evaluation	Count
LOLO	Leave-one-lake-out cross-validation	—

According to radiative transmission mechanism, the R_{rs} is governed by the total absorption coefficients (a) and backscattering coefficients (b_b), which can be expressed as follows [51]:

$$R_{rs} = \frac{ft^2}{Qn^2} \cdot \frac{b_b}{a + b_b} \quad (3)$$

where f is the empirical parameter; t is the transmittance of the air–sea interface; Q is the upwelling irradiance-to-radiance ratio, which is a function of the solar zenith angle and

optical properties of water; n is the real part of the refractive index of water. In addition, a can be decomposed into a_p, a_{cdom}, and pure water absorption a_w:

$$a = a_p + a_{cdom} + a_w \tag{4}$$

The equal-backscattering and comparable-CDOM assumptions used in the derivation are treated as first-order approximations within the calibration domain rather than as invariant optical equalities. Their validity may be affected by phytoplankton fluorescence, non-algal particles, mineral particles, and other optically active constituents in inland waters. The complete 180-record field dataset was subjected to quality-control and component-consistency screening; quantitative component closure was evaluated for records with complete matched optical components.

To eliminate the interference of a_{ph}, a_{CDOM}, and b_b, the band λ_1 and λ_2 is introduced, and it should meet the following assumptions: $b_b(\lambda_1) \approx b_b(\lambda_2)$; $a_{\mathrm{CDOM}}(\lambda_1) \approx a_{\mathrm{CDOM}}(\lambda_2)$. Therefore, the difference between the reciprocal of those two bands can be calculated:

$$\frac{1}{R_{rs}(665)} - \frac{1}{R_{rs}(705)} \approx \frac{Q}{f}\frac{n^2}{t^2}\frac{a_p(665) - a_p(705) + a_w(665) - a_w(705)}{b_b(665)} \tag{5}$$

To further eliminate the interference of b_b, the $\lambda_3 = 740$ nm is also introduced, which should meet the following assumptions: $a(740) \approx a_{\mathrm{w}}(740)$; $b_b(740) \approx b_b(665)$; $a_{\mathrm{w}}(740) \gg b_b(740)$. Therefore, the $R_{rs}(740)$ can be expressed as follows:

$$R_{rs}(740) \approx \frac{f}{Q}\frac{t^2}{n^2}\frac{b_b(740)}{a_w(740)} \tag{6}$$

Combining the Formulas (5) and (6), it can be derived:

$$\left(\frac{1}{R_{rs}(665)} - \frac{1}{R_{rs}(705)}\right) \times R_{rs}(740) = \frac{a_p(665) - a_p(705) + a_w(665) - a_w(705)}{a_w(740)} \tag{7}$$

where $a_w(665)$, $a_w(705)$, and $a_w(740)$ are fixed values.

In addition, an empirical formula $a_p(705) = 1.29 * a_p(665) + 0.223$ can be obtained (Figure S1b). Therefore, following formula can be revised:

$$\left(\frac{1}{R_{rs}(665)} - \frac{1}{R_{rs}(705)}\right) \times R_{rs}(740) = \frac{-0.29 \times a_p(665) + a_w(665) - a_w(705) - 0.223}{a_w(740)} \tag{8}$$

Therefore, the $\mathrm{C_{POC}}$ could be determined by $\left(\frac{1}{R_{rs}(665)} - \frac{1}{R_{rs}(705)}\right) \times R_{rs}(740)$:

$$\mathrm{C_{POC}} \propto \Delta_1 \times a_p(665) \propto \Delta_2 \times \left(\frac{1}{R_{rs}(665)} - \frac{1}{R_{rs}(705)}\right) \times R_{rs}(740) \tag{9}$$

where δ_1 and δ_2 are fixed proportionality coefficients. The three-band index is expressed as $\mathrm{X} = (1/\mathrm{R_{rs}}(665) - 1/\mathrm{R_{rs}}(705)) \times \mathrm{R_{rs}}(740)$.

Synchronous particulate-backscattering measurements were not available; therefore, the equal-backscattering assumptions could not be directly verified. Their potential influence was evaluated using a parameterized sensitivity analysis, in which

$$b_b(\lambda) = b_b(665)(\lambda/665)^{-\eta} \tag{10}$$

and eta was varied from 0 to 3 (Figure S8). The value $\eta = 1.5$ is used only as an illustrative intermediate scenario in the sensitivity test, not as a fitted model parameter. The sensitivity analysis therefore quantifies the potential influence of these assumptions; it does not constitute a validation of the assumptions themselves.

3.1.4. Accuracy Assessment

Three widely recognized statistical metrics, including Mean Absolute Error (MAE), Root Mean Square Error (RMSE), and Mean Absolute Percentage Error (MAPE), were applied to quantify the accuracy of the developed algorithms. These metrics are expressed as follows:

$$\mathrm{MAE} = \frac{1}{n}\sum_{i=1}^{n}\left|C_{POC_{i,m}} - C_{POC_{i,d}}\right| \quad (11)$$

$$\mathrm{RMSE} = \sqrt{\frac{1}{n}\sum_{i=1}^{n}\left(C_{POC_{i,m}} - C_{POC_{i,d}}\right)^2} \quad (12)$$

$$\mathrm{MAPE} \quad \frac{1}{n}\sum_{i=1}^{n}\left(\left|C_{POC_{i,m}} - C_{POC_{i,d}}\right|/C_{POC_{i,m}}\right) * 100\%, \quad (13)$$

where $C_{POC_{i,m}}$ and $C_{POC_{i,d}}$ represent the in-situ and predicted C_{POC}, respectively. In addition, normalized RMSE (nRMSE), Root Mean Square Logarithmic Error (RMSLE), and signed bias are also reported to provide a more comprehensive assessment of model robustness. These metrics are defined as:

$$\mathrm{nRMSE} = \frac{\mathrm{RMSE}}{\overline{C}_{POC,m}} \times 100\% \quad (14)$$

where $\overline{C}_{POC,m}$ is the mean of measured C_{POC}.

$$\mathrm{RMSLE} = \sqrt{\frac{1}{n}\sum_{i=1}^{n}\left[\ln\left(C_{POC_{i,d}} + 1\right) - \ln\left(C_{POC_{i,m}} + 1\right)\right]^2} \quad (15)$$

Predictive R^2 was calculated from the paired measured and predicted values in each evaluation set as follows [52]:

$$R^2 = 1 - \frac{\sum_{i=1}^{N}(y_i - \hat{y}_i)^2}{\sum_{i=1}^{N}(y_i - \bar{y})^2} \quad (16)$$

Here, y_i and $\hat{y}_i$ are the measured and predicted C_{POC} for record i, $\bar{y}$ is the mean measured C_{POC} in the corresponding evaluation set, and N is the number of paired records. Equation (16) evaluates the model predictions directly; it is not the squared correlation of a secondary fitted regression through the scatter. A negative R^2 indicates larger squared prediction error than the evaluation-set mean reference, even when all concentrations are nonnegative.

For the LOLO diagnostic shown in Figure S9, a nonnegative concentration constraint was applied before plotting and evaluation. The nonnegative values shown in that figure therefore should not be described as negative concentration predictions. RMSLE uses nonnegative inputs.

$$\mathrm{Bias} = \frac{1}{n}\sum_{i=1}^{n}\left(C_{POC_{i,d}} - C_{POC_{i,m}}\right) \quad (17)$$

Measured-versus-predicted scatter plots were used to inspect agreement with the 1:1 line. Where shown, an ordinary least-squares line summarizes the scatter and does not replace predictive R^2. In LOLO evaluation, each lake represented in the diagnostic dataset was withheld in turn, the empirical closure was recalibrated using the remaining lakes, and predictions were generated for the withheld lake. The held-out predictions were pooled once to calculate the overall metrics in Figure S9, and were also evaluated separately by lake (Table S6). N is the number of paired measured and predicted observations used in the stated calculation; it is not the number of lakes.

3.2. Independent Estuarine Transfer Testing

To evaluate the transferability of the developed models, two independent estuarine datasets with high turbidity and strong anthropogenic impact were additionally compiled: the Pearl River Estuary (N = 17) and the Rongjiang Estuary (N = 13; Figure S2). These two estuarine datasets are used exclusively as an external transferability test of the finalized algorithm rather than as a substitute for a fully independent global validation. The accuracy metrics defined in Section 3.1.4 were also used to summarize performance in these independent datasets.

3.3. Comparison with Published Algorithms

Current remote sensing algorithms for estimating C_{POC} can be broadly categorized into three main types: (1) empirical models (Type I), which establish statistical relationships between R_{rs} and in situ C_{POC} measurements; (2) chlorophyll-a-mediated indirect models (Type II), which estimate C_{POC} via intermediate retrieval of chlorophyll-a, suitable for phytoplankton-dominated systems; and (3) semi-analytical models based on inherent optical properties (IOPs, Type III), which leverage radiative transfer theory to invert absorption and scattering coefficients before deriving C_{POC}. These three approaches have been widely applied to marine, estuarine, and some large lake systems, and are increasingly adapted for inland waters with heterogeneous optical conditions. To rigorously evaluate the performance of the proposed algorithm, representative models from each category were recalibrated and tested on a unified dataset for direct comparison.

To benchmark the proposed algorithm, three representative published approaches were selected for comparison: the empirical model of Duan et al. [53], the Maximum Normalized Difference Chlorophyll Index (MNDCI), and the semi-analytical scheme of Lin et al. [11]. Their equations, assumptions, and implementation details are summarized in Table S3. All algorithms requiring local recalibration were estimated on the calibration subset and evaluated on the identical holdout records from the nine field-sampled lakes. A fair comparison was ensured by applying all algorithms to the same reflectance inputs and validation dataset.

3.4. Regional Satellite Application and Driving-Factor Analysis

3.4.1. Sentinel-2 MSI Acquisition and Preprocessing for 90 Lakes

Sentinel-2 MSI has become one of the most widely used sensors for monitoring optically complex inland waters owing to its high spatial resolution and favorable spectral configuration [54,55]. A total of 503 cloud-free MSI Level-1C scenes covering the 90 target lakes were obtained from the Copernicus Data Space Ecosystem (CDSE) and from the Sentinel-2 Level-1C collection available through Google Earth Engine (GEE), which served as complementary data-access routes, for the period 2018–2024; the full scene inventory referred to as Table S5 is provided in the public repository cited in the Data availability statement because it is too large to reproduce in the supplementary document. Initial screening removed pixels contaminated by cloud, cloud shadow, sun glint, cast shadows, or surface cyanobacterial accumulations following procedures described in recent inland-water remote-sensing literature [48,55].

Atmospheric correction was subsequently performed using the dark-spectrum fitting (DSF) algorithm embedded in the ACOLITE 20231023.0 processing package (https://github.com/acolite (accessed on 30 October 2026)), which has been extensively validated for deriving R_rs over turbid coastal and inland waters [56,57]. Lake boundaries were delineated following the approach of Zhang et al. [58], and all corrected scenes were resampled to a uniform 20 m grid to standardize spatial resolution across the analysis. Residual bloom-

affected pixels were flagged and excluded using the Virtual-Baseline Floating macroAlgae Height (VB-FAH) index:

$$VB - FAH = (R_{NIR} - R_{Green}) + (R_{Green} - R_{Red}) \times (\lambda_{NIR} - \lambda_{Green})/2(\lambda_{NIR} - \lambda_{Green} - \lambda_{Red}) \quad (18)$$

where R and λ indicates the R_{rs} and central wavelength of the Sentinel-2 MSI data, respectively.

3.4.2. C_{POC} Retrieval and Temporal Summaries

The in-situ R_{rs} measurements were used to establish and validate the optical relationship underlying the semi-analytical retrieval (Section 3.1); the regional C_{POC} maps were produced by applying the same spectral formulation to atmospherically corrected Sentinel-2 MSI observations (Section 3.4). No strictly synchronous satellite–field matchups were constructed, and the Sentinel-2 application is therefore presented as a regional implementation of a field-calibrated algorithm rather than as an independently validated satellite product.

For temporal compositing, C_{POC} (mg/L) was first retrieved for each valid pixel in each image using the semi-analytical algorithm described in Section 3.1 and calibrated in Equation (19). The retrievals within each target time window (month, season, or year) were aligned to a common 20 m grid. For each grid cell, the composite was the arithmetic mean of the valid C_{POC} estimates available during that time window. A grid cell was retained as missing when no valid observation remained because no usable cloud-free MSI acquisition was available or all candidate observations were excluded by the quality-control masks. No spatial or temporal interpolation was applied to fill these gaps.

The pixel-level C_{POC} maps use a common concentration legend (mg/L) to visualize the calculated monthly, seasonal, or annual means. The color intervals are display intervals, not statistically tested concentration classes. No hypothesis test is inferred from a change in map color, and nearby pixels are not treated as independent replicates. The mapped patterns and temporal differences are interpreted descriptively in view of retrieval uncertainty.

For inter-annual trajectories, annual lake–year values were calculated from the annual mosaics after pixel-level quality screening. For each lake–year, the median of finite pixels was retained only when the valid-area fraction reached at least 30% of that lake's maximum observed finite-pixel extent. Regional annual summaries were then calculated as the median and interquartile range across all qualifying lake–year values for each year. Annual files that were unavailable and available years below the coverage threshold were retained as missing and were not temporally interpolated.

3.4.3. Auxiliary Environmental Datasets

To contextualize C_{POC} dynamics within the broader hydro-meteorological and socioeconomic setting, multi-source ancillary data were assembled for 2018–2024. Annual precipitation totals (mm), mean near-surface air temperature (°C) and annual runoff depth (mm) were retrieved from the China Meteorological Administration (CMA) archive (http://data.cma.cn/ (accessed on 30 October 2026)) after rigorous quality screening and spatial harmonization. Land-cover fractions (cropland, built-up, and vegetation) were derived from ESA WorldCover 2021. Population, fertilizer application, freshwater aquaculture area, and wastewater discharge volumes (metric tons) were compiled from official statistical yearbooks and the National Bureau of Statistics database (http://data.stats.gov.cn/ (accessed on 30 October 2026)). These variables were used as catchment-scale or administrative proxies in the supplementary driving-factor analysis; they were not treated as direct nutrient-load measurements. Land-cover fractions (cropland, built-up, and vegetation) were computed within the lake catchments; population, fertilizer application, freshwater aquaculture area, and wastewater discharge were compiled at the administrative level and matched to each lake's corresponding administrative unit(s).

3.4.4. Driving-Factor Analysis

The regional satellite analysis refers to the 90-lake application set. Driving-factor analysis was performed in two complementary ways. Spearman rank correlations were calculated between C_{POC} and the in-situ meteorological and water-quality variables, together with the auxiliary catchment and human-activity indicators. To quantify spatial differentiation, GeoDetector factor-q statistics were calculated for lake-mean C_{POC} using the retained catchment-scale and human-activity indicators. Continuous predictors were discretized into quantile classes, and significance was assessed with 2000 permutations. All results are interpreted as statistical associations rather than causal effects. The in-situ meteorological and water-quality correlations refer to field observations; the satellite-derived regional patterns refer to the 90-lake application set. The auxiliary catchment and human-activity analysis uses a separate 10-lake, 70-record lake–year panel, as specified in Section 4.4.3.

4. Results

4.1. Algorithm Development and Evaluation in the Nine-Lake Dataset

Calibration on the training subset yielded the following linear relationship between C_{POC} and the three-band index X (Figure 2a):

$$C_{POC} = 10.43 \times \left(\frac{1}{R_{rs}(665)} - \frac{1}{R_{rs}(705)} \right) \times R_{rs}(740) - 0.49 \quad (19)$$

where $X = (1/R_{rs}(665) - 1/R_{rs}(705)) \cdot R_{rs}(740)$ is the three-band index defined in Section 3.1.

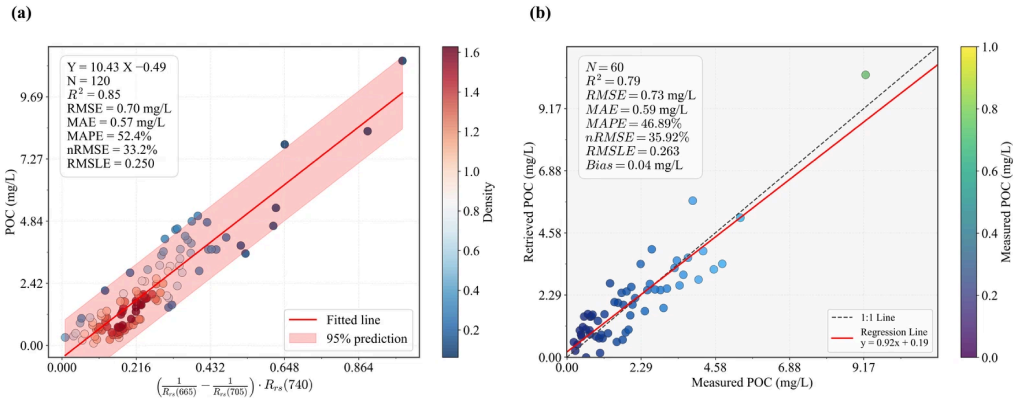


Figure 2. Algorithm development using the calibration subset (**a**) and evaluation using the concentration-stratified holdout subset (**b**). Measured and retrieved C_{POC} are in mg/L; the three-band index is dimensionless. MAE and RMSE are in mg/L; MAPE is in %; R^2 is dimensionless.

Validation against the 60-sample holdout set yielded the following evaluation statistics: MAE = 0.59 mg/L, RMSE = 0.73 mg/L, MAPE = 46.89% (Figure 2b). The measured-versus-predicted scatter showed a linear correspondence between retrieved and measured C_{POC} (slope = 0.92, $R^2 > 0.75$) across the 0.5–5 mg/L range. Percentage errors were most unstable at low concentrations: the 19 samples below 1 mg/L had a MAPE of 84.09%, whereas the single sample above 6 mg/L had an absolute error of 1.19 mg/L and a relative error of 12.85%.

To test transferability to previously unseen lakes, the proposed relationship was evaluated by leave-one-lake-out cross-validation. The pooled out-of-lake predictions yielded R^2 = 0.614, MAE = 0.777 mg/L, RMSE = 1.034 mg/L, nRMSE = 51.07%, RMSLE = 0.308, and mean bias = −0.185 mg/L. The pooled R^2 is below the 0.65 reference discussed by Prairie [59]. Lake-specific performance was heterogeneous, including negative R^2 values (Table S6); Figure S9 shows the pooled concentration predictions, and the pooled statistic

does not imply equal accuracy within every lake. Lake-specific negative R^2 values indicate predictions less accurate than the mean-reference prediction for the corresponding evaluation set. Small sample sizes and restricted concentration ranges may affect the stability of lake-specific R^2, but do not remove these observed limitations. Cross-lake applicability is therefore described as preliminary and heterogeneous within the represented optical and concentration domain. The observation-level holdout R^2 of 0.79 evaluates a different prediction target and does not establish equivalent performance for unseen lakes.

The lake-specific LOLO scores and sample counts are reported in Table S6. These scores refer to the same out-of-lake predictions pooled in Figure S9 and should be distinguished from the concentration-stratified holdout evaluation in Figure 2. Negative lake-specific R^2 values indicate limited predictive performance relative to that lake's mean reference and are retained in the table. The current pooled scatter does not display separate results for each lake.

4.2. Transfer Testing in Independent Estuarine Datasets

Transferability beyond inland lakes was evaluated using two independent estuarine datasets from the Pearl River Estuary (N = 17) and the Rongjiang Estuary (N = 13), both characterized by pronounced turbidity and anthropogenic influence (Figure S2). Error statistics for both systems remained within MAE < 0.8 mg/L, RMSE < 0.85 mg/L, and MAPE < 23% (Figure S3), suggesting that the algorithm has potential for application across optically distinct aquatic environments.

4.3. Comparison with Published Algorithms

When benchmarked against three representative published algorithms on the identical holdout dataset (Figures 3 and S5), the proposed algorithm achieved the highest R^2 (0.79) and the lowest MAE (0.59 mg/L) and RMSE (0.73 mg/L), compared with the Lin semi-analytical model (R^2 = 0.55, MAE = 0.67 mg/L, RMSE = 1.07 mg/L, MAPE = 39.9%), the Duan empirical model (R^2 = 0.01, MAE = 1.10 mg/L, RMSE = 1.59 mg/L, MAPE = 81.8%), and MNDCI (R^2 = −21.84, MAE = 1.37 mg/L, RMSE = 3.94 mg/L, MAPE = 404.6%). The negative MNDCI R^2 indicates out-of-sample performance worse than the mean-reference model (Section 3.1.4).

4.4. Regional Satellite Application and Driving Factors

4.4.1. Seasonal and Inter-Annual C_{POC} Dynamics

Monthly and seasonal C_{POC} composites derived from MSI imagery (Figures 4 and 5) show seasonal variation potentially associated with climate and human activity. Minimum concentrations (1.03–1.41 mg/L) were recorded consistently in January and December, with the lowest values concentrated in the inland portions of Jiangsu, Hubei, and northern Anhui. A sustained spring increase began in March, lifting concentrations to 1.78–2.16 mg/L by April–May. Summer maxima of 4.03–5.90 mg/L were reached in July–August, broadly coinciding with peak phytoplankton productivity and monsoon-driven nutrient flushing across the middle Yangtze and adjacent lake systems. Concentrations retreated to 1.78–2.53 mg/L through the autumn transition (September–November).

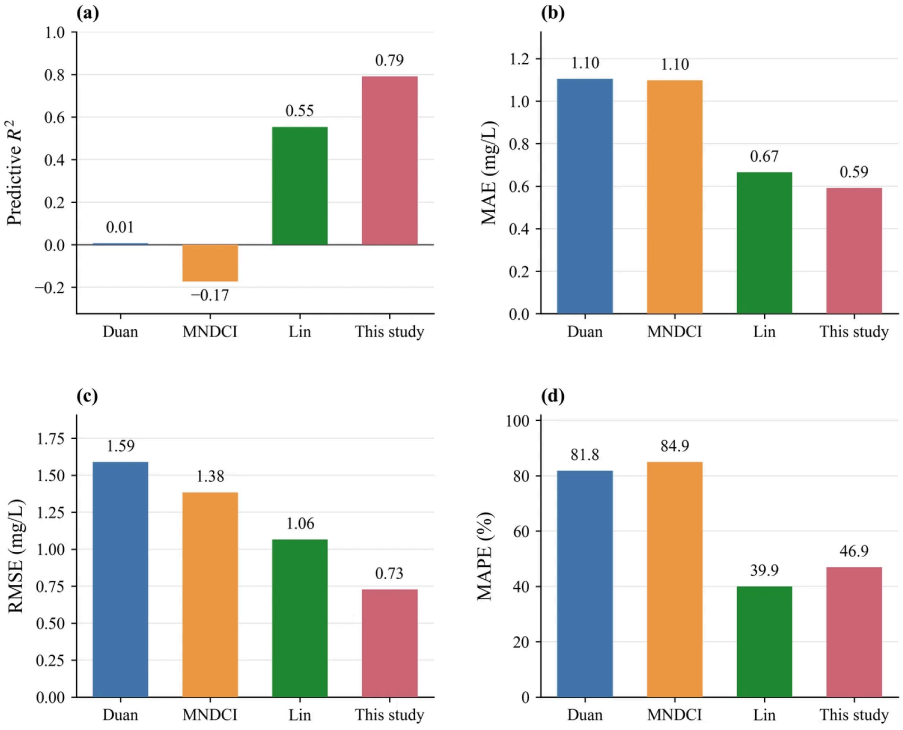


Figure 3. Comparison of the four algorithm implementations using the same validation dataset: Duan et al. [53], MNDCI [21], Lin et al. [11]: (**a**) predictive R^2, (**b**) MAE, (**c**) RMSE, and (**d**) MAPE. R^2 is dimensionless, MAE and RMSE are in mg/L, and MAPE is in %. MNDCI statistics are conditional: they are computed after excluding two high-index extrapolation failures, which are reported separately. The other three algorithms use all available validation records. The evaluation subsets therefore differ among the algorithms shown, and full-set as well as matched-subset metrics are retained in the accompanying calculation records.

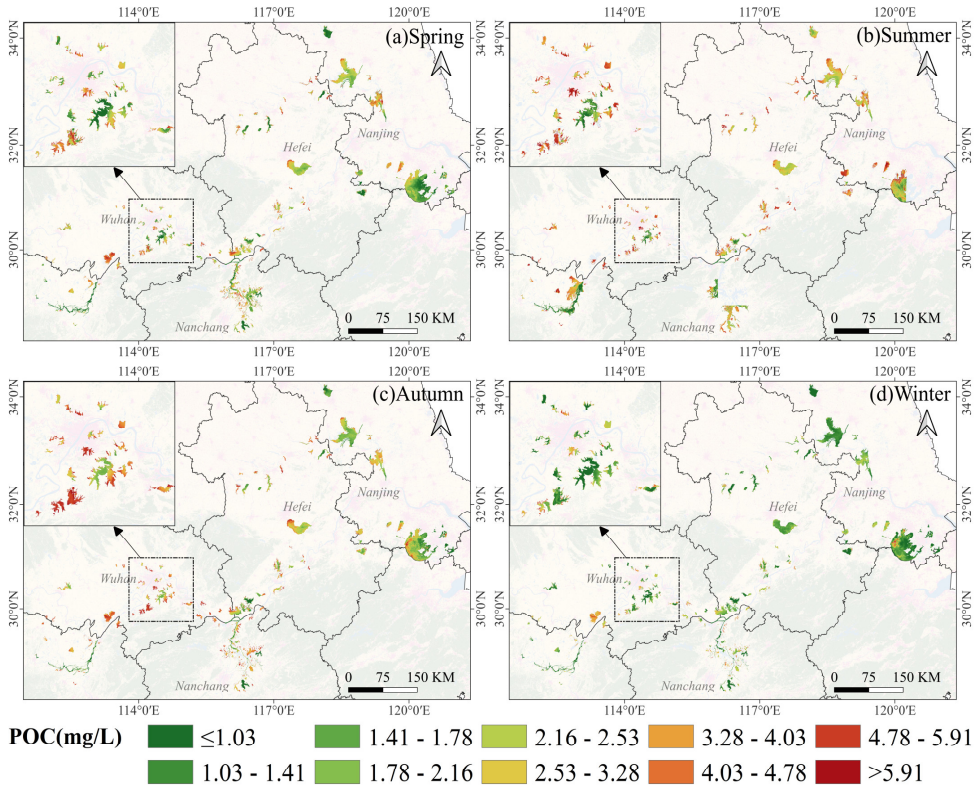


Figure 4. Seasonal mean Sentinel–2–derived particulate organic carbon concentrations (C_{POC}, mg/L) at the pixel scale across the 90–lake application set.

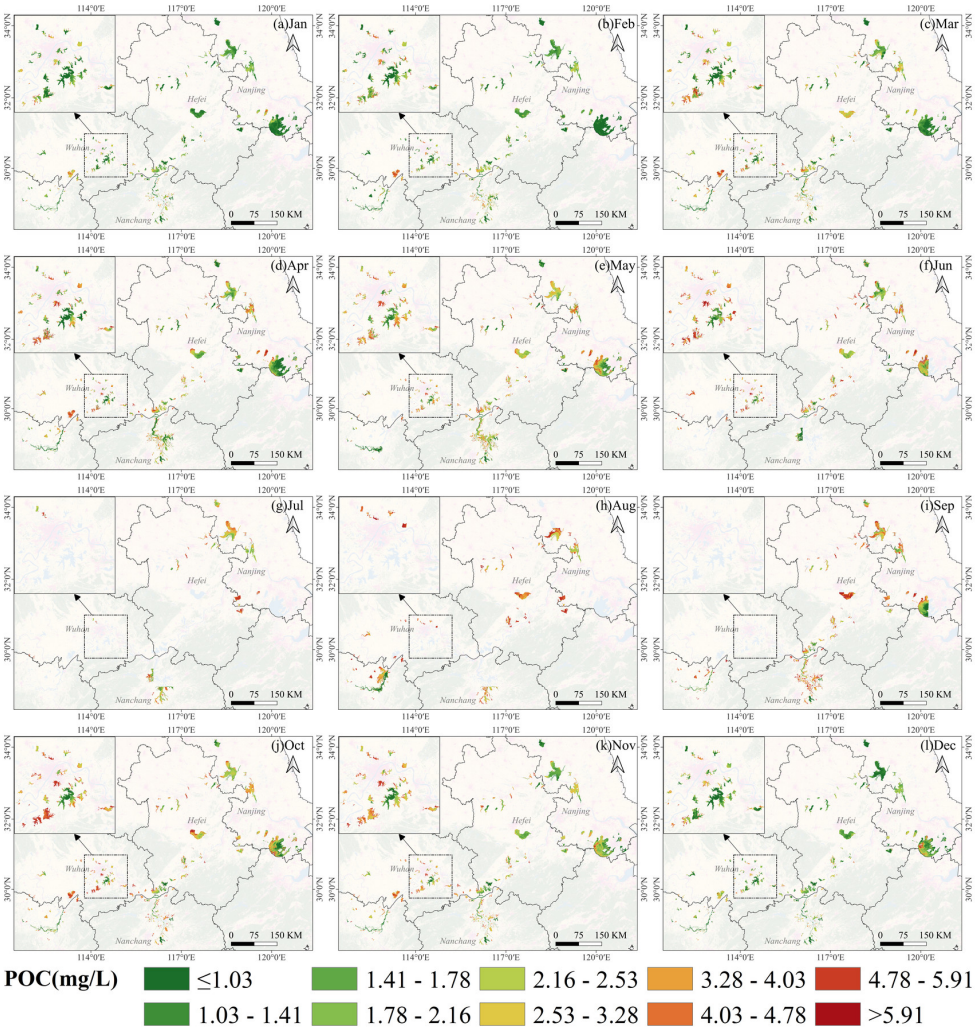


Figure 5. Monthly mean Sentinel-2–derived particulate organic carbon concentrations (C_{POC}, mg/L) at the pixel scale across the 90–lake application set.

Inter-annual trajectories showed substantial year-to-year variability rather than a monotonic regional trend (Figure S11a). These regional summary statistics (see below) should be distinguished from the spatial extent of local high-C_{POC} areas: although the annual maps (Figure S4) show widespread enrichment during 2020 and 2023, with persistent high-C_{POC} areas along the Jiangsu–Hubei corridor, such spatial patterns do not necessarily imply an increase in the regional annual median. The observed interannual variability is therefore interpreted descriptively; potential controls related to hydrological, meteorological, nutrient, and anthropogenic processes require dedicated quantitative attribution beyond the scope of the present study.

The regional annual trajectory (Figure S11a) summarizes the median and inter-lake interquartile range of all qualifying lake–year C_{POC} values. The regional median peaked in 2019, declined in 2020, remained broadly stable during 2021–2022, and decreased further in 2023–2024; the inter-lake IQR indicates persistent spatial heterogeneity. Panels (b)–(g) of Figure S11 show the corresponding trajectories for six a priori selected representative large lakes—Taihu, Chaohu, Hongze, Gaoyou, Poyang, and Dongting—spanning the Yangtze and Huaihe basins and contrasting geographic settings. Unavailable annual files and years below the 30% valid-coverage criterion remain explicitly marked and were not interpolated.

4.4.2. Multi-Scale Spatial Patterns in C_{POC}

At the regional scale, the calculated concentration maps showed an east-to-west and north-to-south decrease across central-eastern China (Figure 6). Peak concentrations (4.03–5.91mg/L) were concentrated in the Nanjing metropolitan environs of Jiangsu Province, declining progressively through Anhui and Hubei before reaching minima below 1.03 mg/L in southern Hunan and Jiangxi. The observed gradient spatially coincides with contrasts in land-use intensity and hydroclimatic conditions across the study region: the industrialized, densely settled eastern and northern catchments contrast with the less anthropogenically modified south, where heavier precipitation and stronger riverine dilution—particularly through the Yangtze main channel—disperse and attenuate the particulate carbon signal.

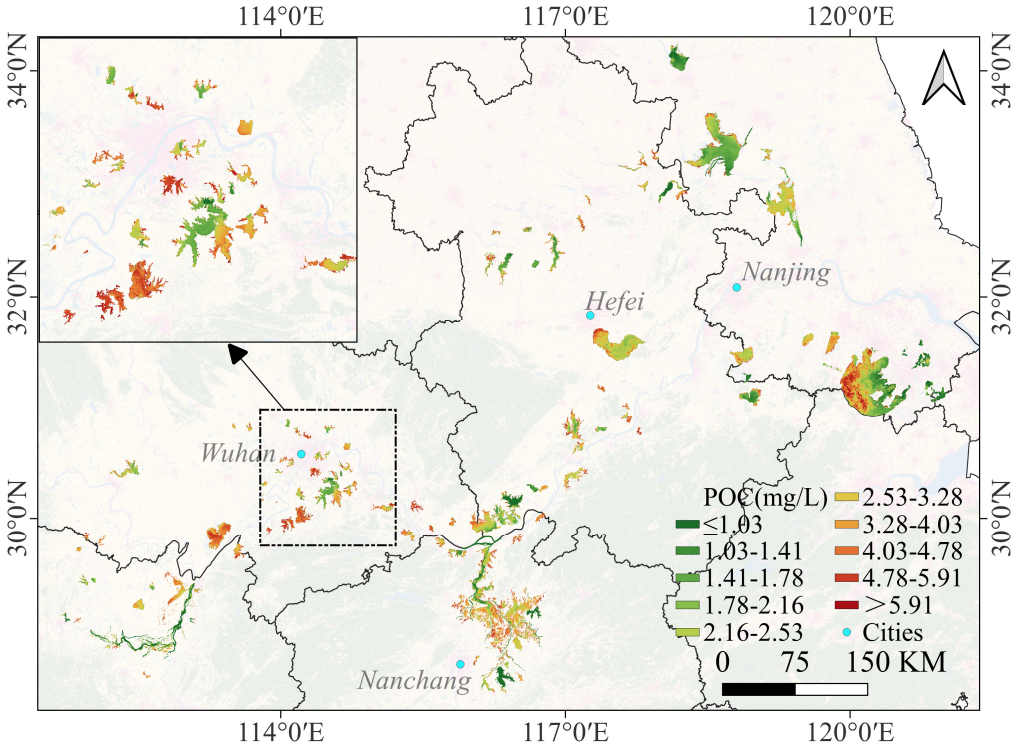


Figure 6. Mean Sentinel–2–derived C_{POC} concentrations (mg/L) at the pixel scale across the 90–lake application set during 2018–2024. Color intervals visualize calculated concentrations and do not denote statistically distinct classes.

At the city-lake scale, persistent hotspots were identified in water bodies adjacent to Wuhan, Nanjing, and Hefei, where C_{POC} regularly exceeded 5 mg/L [60,61]. The co-occurrence of agricultural runoff, industrial effluent discharge, and organic waste accumulation in these settings creates compounding nutrient and carbon loading. Conversely, lakes near Changsha and Nanchang maintained lower C_{POC} (1.03–1.78 mg/L), consistent with stronger hydrological flushing and lower anthropogenic pressure.

Within individual lakes, the maps showed within-lake concentration gradients that may be associated with hydrodynamic conditions. Both Lake Chaohu and Lake Hongze displayed elevated C_{POC} in their northern sectors, reflecting preferential deposition of terrigenous organic matter delivered by northern tributaries [62]. Lake Taihu exhibited an inverse west-to-east gradient, with elevated C_{POC} concentrations in the western embayments, a pattern consistent with previously reported wind-driven circulation dynamics that promote the accumulation of suspended organic matter in sheltered regions. In the more centrally positioned Lake Dongting and Lake Poyang, localized concentration anomalies

track seasonal bank erosion and variable tributary discharge, redistributing the particulate carbon pool within the lake basins.

4.4.3. Driving-Factor Results

Among the environmental variables examined in the pooled field dataset, C_{Chla} showed the strongest Spearman association with C_{POC} ($\rho = 0.79$; Figures 7A and S6), followed by atmospheric pressure ($\rho = -0.67$) and C_{TP} ($\rho = 0.54$). C_{TN} showed a weak monotonic association with C_{POC} ($\rho = -0.15$), and water temperature showed a moderate positive association ($\rho = 0.38$). These statistics use pairwise-complete field observations, rather than lake means, and are treated as descriptive associations. The catchment and human-activity correlations in Figure 7B use the separate 10-lake, 70-record lake–year panel. GeoDetector identified cropland fraction ($q = 0.588$, $p = 0.0495$) and annual precipitation ($q = 0.573$, $p = 0.0370$) as the strongest exploratory spatial associations among the catchment and human-activity indicators (Figure 8); the remaining retained factors had $q \leq 0.267$ and $p \geq 0.56$. These statistics describe statistical associations within the analyzed dataset and do not establish causal effects.

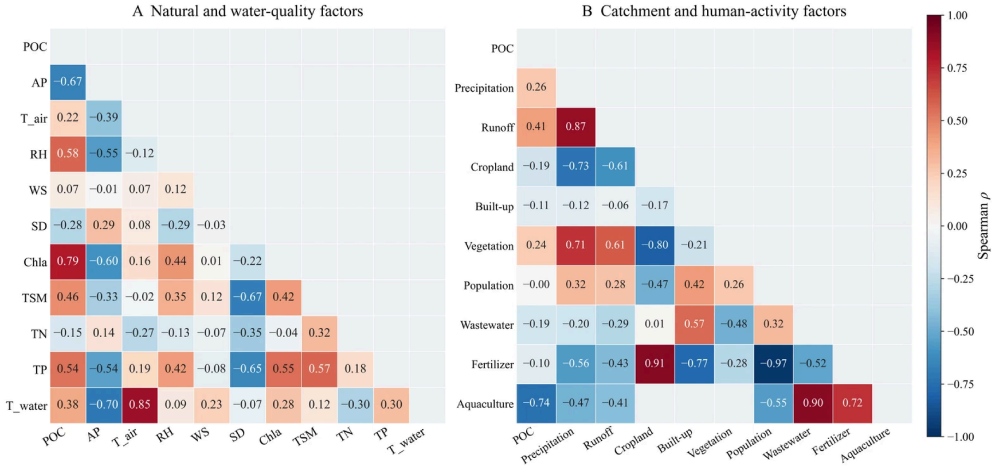


Figure 7. Spearman rank correlations between C_{POC} and (**A**) field meteorological and water-quality variables and (**B**) catchment and human-activity indicators. Correlation coefficients are dimensionless.

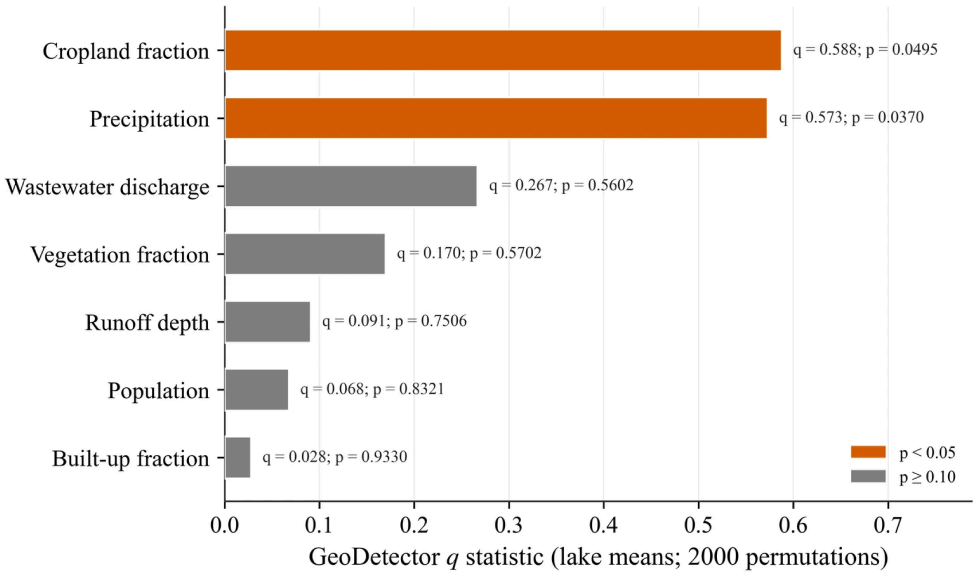


Figure 8. GeoDetector q statistics for the retained catchment and human-activity indicators. Both q and the displayed p values are dimensionless.

5. Discussion

5.1. Nine-Lake Algorithm Development and Evaluation

The retrieval scheme presented here achieves a favorable balance between physical interpretability and operational practicality. By anchoring on $a_p(665)$—a quantity mechanistically linked to the particulate carbon pool—the algorithm avoids the empirical fragility of pure statistical approaches while sidestepping the computational overhead of full IOP inversion. The three-band formulation at 665, 705, and 740 nm simultaneously captures the particulate absorption peak near 665 nm and suppresses a_{cdom} and b_b interference through differencing operations, ensuring that the retrieved signal reflects genuine biogeochemical variation rather than optical artifacts. This design showed useful but non-uniform cross-lake applicability across the sampled lakes: performance was strongest over much of the sampled trophic and optical gradient but remained heterogeneous among individual lakes (Section 4.1).

Nonetheless, the linear regression closure imposes known constraints. Spectral saturation and multiple-scattering effects distort the red and NIR reflectance signal at $C_{POC} > 6$ mg/L, while at $C_{POC} < 1$ mg/L the weak absorption signal approaches the sensor noise floor—particularly in waters where chlorophyll-a fluorescence dominates the optical budget. Both regimes produce systematic retrieval biases. Additionally, spectral overlap between a_p and chlorophyll-a fluorescence can inject non-biogenic bias during intense bloom events [2,36], especially in shallow, stratified lakes where subsurface vertical heterogeneity perturbs the water-leaving radiance. Future developments may benefit from hybrid physics-informed learning frameworks that combine radiative-transfer constraints with nonlinear representation learning, thereby improving generalization while preserving physical consistency.

The holdout RMSE of 0.73 mg/L indicates appreciable uncertainty for individual predictions, particularly at low concentrations. Twice this RMSE is 1.46 mg/L; this gives a rough scale of individual prediction uncertainty only under suitable assumptions about residual bias, variance, and distribution. It is not by itself a calibrated 95% prediction interval or a test of the difference between two predictions. Accordingly, the present results do not establish statistically distinct fine concentration classes or significant differences between adjacent map-color intervals [52,59].

These concentration-dependent effects define the boundary conditions of the linear closure rather than evidence of wholesale model failure. The low-and high-concentration observations are retained in the analysis, but uncertainty should be interpreted as higher at the distribution tails. Accordingly, the present algorithm is intended for regional monitoring within the optical and concentration domain represented by the sampled YHP large lakes. Future work should expand the number of observations at the low-and high-concentration tails and acquire synchronous measurements of particulate backscattering and other optical components; broader deployment should be preceded by independent testing and, where necessary, nonlinear or segmented recalibration.

The optical assumptions should therefore be interpreted as first-order approximations rather than universal identities. The method remains applicable within the sampled YHP lake domain, but uncertainty may increase in waters with optical compositions outside the calibration domain. Independent validation is warranted for strongly particle-dominated, mineral-rich, or otherwise optically distinct waters.

The concentration-stratified holdout evaluates observation-level prediction within the sampled lake assemblage, but samples from the same lake or sampling campaign may occur in both subsets. LOLO removes overlap with the test lake by withholding every observation from that lake during calibration, yielding pooled $R^2 = 0.614$ and heterogeneous lake-specific performance. No temporally blocked validation was performed; training and testing across

lakes may share seasons or years. Neither evaluation establishes predictive transferability to future years or unseen sampling campaigns. Applications to unrepresented lakes should therefore be interpreted cautiously and evaluated independently.

The algorithm also showed encouraging performance when applied to two independent estuarine datasets; these results should be interpreted as preliminary evidence of transferability rather than comprehensive validation.

5.2. Comparison with Published Algorithms

The benchmark comparison (Section 4.3 and Figure 3) showed that the proposed algorithm achieved the highest R^2, surpassing the Lin model and substantially exceeding the Duan and MNDCI schemes. The Lin model's comparatively strong showing reflects its multi-band IOP inversion, which partially mitigates non-algal particulate interference—an advantage in turbid, eutrophic settings like Lake Taihu. The MNDCI approach, calibrated primarily for phytoplankton-rich open-water environments, is sensitive to accurate C_{Chla} retrieval and degrades wherever sediment resuspension or allochthonous organic inputs weaken the C_{POC}–C_{Chla} coupling [11,25]. The Duan empirical model exhibits high sensitivity to local optical properties and shows stronger sensitivity to local optical conditions, which may limit cross-lake transferability. The improved performance is likely associated with its targeted suppression of suspended particulate matter interference in the MSI red-edge and NIR channels, combined with explicit dampening of $a_{CDOM}(\lambda)$ and surface reflection contributions. The proposed algorithm also performed well across contrasting lake systems, including Lake Taihu and Lake Chaohu, although lake-specific performance remained heterogeneous (Section 4.1).

5.3. Regional Application and Driving Factors

5.3.1. Spatial Monitoring and Satellite Validation Scope

The 10–20 m spatial footprint of Sentinel-2 MSI confers an additional practical advantage. Coarser sensors such as MODIS (250–500 m) and OLCI (300 m) cannot resolve the intra-lake gradients documented in Section 4.4.2; at those resolutions, shore-proximal hotspots and bay-scale heterogeneity are effectively invisible. The MSI-based approach therefore expands the monitoring perimeter to include small-and medium-sized lakes that have historically been excluded from satellite carbon assessments [32,33].

No strictly synchronous satellite–field matchups were constructed. The regional application therefore represents implementation of a field-calibrated algorithm rather than an independently validated satellite product.

5.3.2. Environmental Associations

Among the suite of environmental variables examined, C_{Chla} showed the strongest Spearman association with C_{POC} ($\rho = 0.79$; Figures 7 and S6). This coupling is mechanistically grounded: phytoplankton photosynthesis is the dominant autochthonous source of POC in eutrophic lakes, and elevated biomass directly augments the particulate carbon inventory [63–65]. The biological pump's efficiency is, in turn, conditioned by nutrient availability. C_{TP} showed the second strongest association among the water-quality variables ($\rho = 0.54$; Figure S7), consistent with the well-established phosphorus-limitation paradigm in freshwater systems [66]: phosphorus scarcity and its complex geochemical cycling routinely impose the proximate constraint on primary production in lakes and estuaries [67]. By contrast, C_{TN} showed no clear monotonic association with C_{POC} ($\rho = -0.15$); this weak association indicates that no clear monotonic relationship was detected between the two variables in the analyzed dataset, and does not necessarily imply that nitrogen availability

is ecologically unimportant, as the diversity of nitrogen chemical species and their rapid interconversions may obscure any direct biogeochemical linkage [68].

Looking beyond nutrient stoichiometry, phytoplankton community composition introduces an additional layer of complexity. Competitive dynamics between diatoms and cyanobacteria, for example, can substantially alter the sinking efficiency of the biological pump, with implications for the vertical partitioning of the POC pool [69]. Climate-driven shifts in community structure [70,71] therefore need to be incorporated into future C_{POC} projections alongside conventional nutrient and temperature forcing.

Turning to physical drivers, water temperature exhibited a moderate positive association with C_{POC} ($\rho = 0.38$) [72,73]. Elevated temperatures stimulate heterotrophic microbial activity, accelerating the decomposition of organic particles into dissolved inorganic carbon and CO_2 and thereby shrinking the POC pool [74]. Concurrently, thermal stratification intensifies under warmer conditions, restricting vertical mixing [75] and curtailing the upward flux of nutrients that would otherwise sustain surface-layer primary production. Although these processes would tend to reduce C_{POC}, the observed positive association most likely reflects seasonal co-variation between warm, productive conditions and peak phytoplankton biomass rather than a direct causal effect; temperature-driven decomposition and stratification effects may act in the opposite direction and cannot be separated in the present correlational design. Atmospheric pressure showed the strongest association among the meteorological variables ($\rho = -0.67$), functioning as a proxy for synoptic weather regimes rather than exerting a direct physicochemical effect: high-pressure anticyclonic conditions bring clear skies, reduced wind stress, and strengthened stratification, collectively suppressing nutrient resupply from deeper water layers and dampening phytoplankton growth.

5.3.3. Implications for Lake Management and Carbon Accounting

The spatiotemporal C_{POC} patterns documented here carry direct operational relevance for lake stewardship. Elevated C_{POC} accelerates eutrophication feedbacks—fueling algal proliferation, depleting hypolimnetic oxygen, and degrading water quality in ways that threaten aquatic biodiversity and compromise ecosystem services. The trajectory of Lake Taihu is instructive: summer C_{POC} enrichment has been closely associated with intensifying cyanobacterial bloom events, with documented consequences for municipal drinking-water supply and ecological integrity [76]. Beyond water-quality management, the POC pool mediates both short-term biological productivity and multi-decadal carbon sequestration in lake sediments, linking inland-water carbon dynamics to regional greenhouse-gas budgets and climate-adaptation planning [9,77].

The retrieval scheme developed here provides an infrastructure for sustained, spatially explicit surveillance of these dynamics across the 90-lake YHP network. Its depiction of areas with relatively high calculated CPOC can help identify locations for subsequent field investigation and management assessment [78]—particularly in rapidly urbanizing catchments where non-point-source agricultural runoff and urban drainage are likely important contributors to C_{POC} enrichment. Coupling the algorithm output with process-based biogeochemical models would further enable scenario-based assessments of lake carbon storage under projected land-use and climate trajectories [8,79]. Independent satellite–field validation and uncertainty assessment are needed before these estimates are used for operational decisions or quantitative carbon accounting.

6. Conclusions

A semi-analytical Sentinel-2 MSI algorithm was developed to retrieve C_{POC} across eutrophic inland waters and applied to 90 lakes in the Yangtze–Huaihe Plain during 2018–2024. By linking a three-band reflectance index to particulate absorption at 665 nm, the algo-

rithm achieved $R^2 = 0.79$, MAE = 0.59 mg/L, RMSE = 0.73 mg/L, and MAPE = 46.89% in the concentration-stratified holdout evaluation. The additional LOLO diagnostic gave pooled $R^2 = 0.614$ and heterogeneous lake-specific performance, indicating that cross-lake applicability remains limited. The regional maps describe spatial and temporal variation in calculated C_{POC}, while the environmental analyses identify statistical associations. Given the individual prediction errors and the absence of strictly synchronous satellite–field matchups, fine concentration differences and adjacent map-color intervals should not be interpreted as statistically distinct classes. Further independent validation is required before the satellite estimates are used for operational management or quantitative carbon accounting.

Supplementary Materials: The following supporting information can be downloaded at: https://www.mdpi.com/article/10.3390/rs18213812/s1, Figure S1: Correlations between particulate organic carbon concentration and inherent optical properties, and the relationship between particulate absorption coefficients at 665 and 705 nm; Figure S2: Locations and sampling sites in the Pearl River Estuary and Rongjiang Estuary; Figure S3: Algorithm performance in the Pearl River Estuary and Rongjiang Estuary; Figure S4: Annual mean Sentinel-2-derived particulate organic carbon concentrations at the pixel scale; Figure S5: Comparison of measured and retrieved particulate organic carbon concentrations for the Duan, MNDCI, Lin, and proposed algorithms; Figure S6: Residual analysis for the four compared algorithms; Figure S7: Relationships between particulate organic carbon concentration and measured environmental variables; Figure S8: Sensitivity to the particulate-backscattering spectral slope; Figure S9: Pooled leave-one-lake-out evaluation of the proposed algorithm; Figure S10: In situ remote-sensing reflectance spectra of the nine field-sampled lakes; Figure S11: Regional and lake-specific annual particulate organic carbon concentrations and their spatial variability; Table S1: Geographical characteristics, sampling information, meteorological data, and mean particulate organic carbon concentrations of the nine sampling lakes; Table S2: The descriptions and corresponding abbreviations used in this paper; Table S3: Equations, assumptions, and implementation notes for the compared algorithms; Table S4: Summary of cloud-free Sentinel-2 images used in the study during 2018–2024; Table S5: Full Sentinel-2 scene inventory available in the public repository; Table S6: Lake-specific scores for the leave-one-lake-out evaluation.

Author Contributions: P.C.: Software, Conceptualization, Methodology, Investigation, Writing—Original Draft, Writing—Review and Editing; X.Z.: Software, Resources, Visualization; H.L.: Software, Investigation, Visualization; S.Z.: Investigation, Visualization; S.L.: Investigation; G.L.: Resources; Y.R.: Validation, Methodology, Writing—Review and Editing, Funding acquisition. All authors have read and agreed to the published version of the manuscript.

Funding: This research received funding from the Youth Foundation for Humanities and Social Sciences of the Ministry of Education of China (23YJC630145), the National Natural Science Foundation of China (42371406 and 42401518), the Natural Science Foundation of Guangdong Province (2025A1515011066), Zhejiang Provincial Water Conservancy Engineering Scientific Research Ranking Project (Grant No. RA+202501) and the Jiangxi Provincial Key Laboratory of Water Ecological Conservation in Headwater Regions (WEC-2024-02).

Data Availability Statement: The processed lake–year driver dataset, analysis scripts, source metadata, and aggregate statistical results have been assembled in a release package prepared for public deposition. The package has been deposited in https://doi.org/10.5281/zenodo.23273401. The full Sentinel-2 scene inventory referred to as Table S5 is also available in this repository. Original station-level field observations are not publicly available and are excluded from the release package. Aggregate field-correlation statistics are supplied, but that component cannot be fully reproduced from the public package alone. Sentinel-2 imagery is publicly accessible through the Copernicus Data Space Ecosystem and Google Earth Engine.

Acknowledgments: We acknowledge the European Space Agency (ESA), the Copernicus Data Space Ecosystem, and the Google Earth Engine platform for providing access to the Sentinel-2 MSI data used in this study, and the China Meteorological Data Sharing Service System (https://data.cma.cn/) for providing the hydro-meteorological data.

Conflicts of Interest: The authors declare no conflicts of interest.

References

1. Liu, D.; Sun, Z.; Shen, M.; Tian, L.; Yu, S.; Jiang, X.; Duan, H. Three-dimensional observations of particulate organic carbon in shallow eutrophic lakes from space. *Water Res*. **2023**, *229*, 119519. [CrossRef]
2. Zhao, Z.; Cai, X.; Huang, C.; Shi, K.; Li, J.; Jin, J.; Yang, H.; Huang, T. A novel semianalytical remote sensing retrieval strategy and algorithm for particulate organic carbon in inland waters based on biogeochemical-optical mechanisms. *Remote Sens. Environ*. **2022**, *280*, 113213. [CrossRef]
3. Bressac, M.; Laurenceau-Cornec, E.C.; Kennedy, F.; Santoro, A.E.; Paul, N.L.; Briggs, N.; Carvalho, F.; Boyd, P.W. Decoding drivers of carbon flux attenuation in the oceanic biological pump. *Nature* **2024**, *633*, 587–593. [CrossRef]
4. Kharbush, J.J.; Close, H.G.; Van Mooy, B.A.S.; Arnosti, C.; Smittenberg, R.H.; Le Moigne, F.A.C.; Mollenhauer, G.; Scholz-Böttcher, B.; Obreht, I.; Koch, B.P.; et al. Particulate Organic Carbon Deconstructed: Molecular and Chemical Composition of Particulate Organic Carbon in the Ocean. *Front. Mar. Sci*. **2020**, *7*, 518. [CrossRef]
5. Cavan, E.L.; Trimmer, M.; Shelley, F.; Sanders, R. Remineralization of particulate organic carbon in an ocean oxygen minimum zone. *Nat. Commun*. **2017**, *8*, 14847. [CrossRef]
6. Ramondenc, S.; Eveillard, D.; Metfies, K.; Iversen, M.H.; Nothig, E.M.; Piepenburg, D.; Hasemann, C.; Soltwedel, T. Unveiling pelagic-benthic coupling associated with the biological carbon pump in the Fram Strait (Arctic Ocean). *Nat. Commun*. **2025**, *16*, 840. [CrossRef]
7. Xu, J.; Li, Y.; Lyu, H.; Lei, S.; Mu, M.; Bi, S.; Xu, J.; Xu, X.; Miao, S.; Li, L.; et al. Simultaneous inversion of concentrations of POC and its endmembers in lakes: A novel remote sensing strategy. *Sci. Total Environ*. **2021**, *770*, 145249. [CrossRef]
8. Liu, D.; Shi, K.; Chen, P.; Yan, N.; Ran, L.; Kutser, T.; Tyler, A.N.; Spyrakos, E.; Woolway, R.I.; Zhang, Y.; et al. Substantial increase of organic carbon storage in Chinese lakes. *Nat. Commun*. **2024**, *15*, 1–9. [CrossRef]
9. Liu, D.; Yu, S.; Wilson, H.; Shi, K.; Qi, T.; Luo, W.; Duan, M.; Qiu, Z.; Duan, H. Mapping particulate organic carbon in lakes across China using OLCI/Sentinel-3 imagery. *Water Res*. **2024**, *250*, 121034. [CrossRef]
10. Middelburg, J.J. Closing the inland water carbon cycle. *Science advance* **2024**, *10*,*eadt3893*. [CrossRef]
11. Lin, J.; Lyu, H.; Miao, S.; Pan, Y.; Wu, Z.; Li, Y.; Wang, Q. A two-step approach to mapping particulate organic carbon (POC) in inland water using OLCI images. *Ecol. Indic*. **2018**, *90*, 502–512. [CrossRef]
12. Stramski, D.; Joshi, I.; Reynolds, R.A. Ocean color algorithms to estimate the concentration of particulate organic carbon in surface waters of the global ocean in support of a long-term data record from multiple satellite missions. *Remote Sens. Environ*. **2022**, *269*, 112776. [CrossRef]
13. Xu, J.; Lei, S.; Bi, S.; Li, Y.; Lyu, H.; Xu, J.; Xu, X.; Mu, M.; Miao, S.; Zeng, S.; et al. Tracking spatio-temporal dynamics of POC sources in eutrophic lakes by remote sensing. *Water Res*. **2020**, *168*, 115162. [CrossRef]
14. Jiang, J.; Chen, Z.; Sun, K.; Chen, Y.; Mu, M.; Sun, Q.; Zeng, S. Monitoring 36-year water clarity dynamics in turbid waters of the Pearl River Estuary, China, using Landsat data. *Ecol. Inform*. **2024**, *81*, 102600. [CrossRef]
15. Zeng, S.; Lei, S.; Li, Y.; Lyu, H.; Dong, X.; Li, J.; Cai, X. Remote monitoring of total dissolved phosphorus in eutrophic Lake Taihu based on a novel algorithm: Implications for contributing factors and lake management. *Environ. Pollut*. **2022**, *296*, 118740. [CrossRef]
16. Zhang, Z.; Liu, H.; He, X.; Zhang, Y.; Wang, Y.; Wang, Y.; Liang, F.; Li, Q.; Wu, G. Satellite retrieval of oceanic particulate organic carbon: Towards an accurate and seamless dataset for the global ocean. *Sci. Total Environ*. **2024**, *955*, 176910. [CrossRef]
17. Cai, S.; Wu, M.; Le, C. Satellite Observation of the Long-Term Dynamics of Particulate Organic Carbon in the East China Sea Based on a Hybrid Algorithm. *Remote Sens*. **2022**, *14*, 3220. [CrossRef]
18. Jiang, G.; Ma, R.; Loiselle, S.A.; Duan, H.; Su, W.; Cai, W.; Huang, C.; Yang, J.; Yu, W. Remote sensing of particulate organic carbon dynamics in a eutrophic lake (Taihu Lake, China). *Sci. Total Environ*. **2015**, *532*, 245–254. [CrossRef]
19. Xue, K.; Ma, R.; Wang, M.; Wei, X.; Liu, H.; Hu, M.; Jiang, L.; Shen, M.; Cao, Z. A state-of-art algorithm to retrieve particulate organic carbon concentration in optically complex waters via multiple satellite missions. *Remote Sens. Environ*. **2025**, *329*, 114914. [CrossRef]
20. Yu, G.; Zhong, Y.; Liu, S.; Lao, Q.; Chen, C.; Fu, D.; Chen, F. Remote Sensing Estimates of Particulate Organic Carbon Sources in the Zhanjiang Bay Using Sentinel-2 Data and Carbon Isotopes. *Remote Sens*. **2023**, *15*, 3768. [CrossRef]
21. Lyu, H.; Wang, Y.; Jin, Q.; Shi, L.; Li, Y.; Wang, Q. Developing a semi-analytical algorithm to estimate particulate organic carbon (POC) levels in inland eutrophic turbid water based on MERIS images: A case study of Lake Taihu. *Int. J. Appl. Earth Obs. Geoinf*. **2017**, *62*, 69–77. [CrossRef]
22. Jiao, W.; Wang, S.; Sun, D.; Lang, S.; Jia, Y.; Wang, L. Estimating two-decadal variations of global oceanic particulate organic carbon using satellite observations and machine learning approaches. *Int. J. Appl. Earth Obs. Geoinf*. **2025**, *137*, 104438. [CrossRef]

23. Sathyendranath, S.; Stuart, V.; Nair, A.; Oka, K.; Nakane, T.; Bouman, H.; Forget, M.H.; Maass, H.; Platt, T. Carbon-to-chlorophyll ratio and growth rate of phytoplankton in the sea. *Mar. Ecol. Prog. Ser.* **2009**, *383*, 73–84. [CrossRef]
24. Son, Y.B.; Gardner, W.D.; Mishonov, A.V.; Richardson, M.J. Multispectral remote-sensing algorithms for particulate organic carbon (POC): The Gulf of Mexico. *Remote Sens. Environ.* **2009**, *113*, 50–61. [CrossRef]
25. Ni, H.G.; Lu, F.H.; Luo, X.L.; Tian, H.Y.; Zeng, E.Y. Riverine inputs of total organic carbon and suspended particulate matter from the Pearl River Delta to the coastal ocean off South China. *Mar. Pollut. Bull.* **2008**, *56*, 1150–1157. [CrossRef]
26. Liu, W.; Lü, H.; Zhu, Y.; Wang, X.; Gao, P.; Su, J. The performance of IMERG near-real-time estimations during the record-breaking Meiyu season in 2020. *J. Hydrol.* **2024**, *634*, 131024. [CrossRef]
27. Song, L.; Song, C.; Zhan, P.; Chen, T.; Liu, K.; Jing, H. Seasonal Amplitude of Water Storage Variations of the Yangtze–Huai Plain Lake Group: Implicaion for Floodwater Storage Capacity. *Front. Environ. Sci.* **2022**, *10*, 838883. [CrossRef]
28. Qi Guan, L.F.; Hou, X.; Schurgers, G.; Zheng, Y.; Tang, J. Eutrophication changes in fifty large lakes on the Yangtze Plain of China derived from MERIS and OLCI observations. *Remote Sens. Environ.* **2020**, *246*, 111890. [CrossRef]
29. Shi, K.; Zhang, Y.; Zhou, Y.; Liu, X.; Zhu, G.; Qin, B.; Gao, G. Long-term MODIS observations of cyanobacterial dynamics in Lake Taihu: Responses to nutrient enrichment and meteorological factors. *Sci. Rep.* **2017**, *7*, 40326. [CrossRef]
30. Ansper, A.; Alikas, K. Retrieval of Chlorophyll a from Sentinel-2 MSI Data for the European Union Water Framework Directive Reporting Purposes. *Remote Sens.* **2018**, *11*, 64. [CrossRef]
31. Chen, L.; Liu, L.; Liu, S.; Shi, Z.; Shi, C. The Application of Remote Sensing Technology in Inland Water Quality Monitoring and Water Environment Science: Recent Progress and Perspectives. *Remote Sens.* **2025**, *17*, 667. [CrossRef]
32. Tavora, J.; Jiang, B.; Kiffney, T.; Bourdin, G.; Gray, P.C.; Carvalho, L.S.; Hesketh, G.; Schild, K.M.; Souza, L.F.; Brady, D.C.; et al. Recipes for the Derivation of Water Quality Parameters Using the High-Spatial-Resolution Data from Sensors on Board Sentinel-2A, Sentinel-2B, Landsat-5, Landsat-7, Landsat-8, and Landsat-9 Satellites. *J. Remote Sens.* **2023**, *3*, 49. [CrossRef]
33. Topp, S.N.; Pavelsky, T.M.; Jensen, D.; Simard, M.; Ross, M.R.V. Research Trends in the Use of Remote Sensing for Inland Water Quality Science: Moving Towards Multidisciplinary Applications. *Water* **2020**, *12*, 169. [CrossRef]
34. Wang, X.; Jiang, Y.; Jiang, M.; Cao, Z.; Li, X.; Ma, R.; Xu, L.; Xiong, J. Estimation of Total Phosphorus Concentration in Lakes in the Yangtze-Huaihe Region Based on Sentinel-3/OLCI Images. *Remote Sens.* **2023**, *15*, 4487. [CrossRef]
35. Xu, J.; Jin, G.; Tang, H.; Zhang, P.; Wang, S.; Wang, Y.G.; Li, L. Assessing temporal variations of Ammonia Nitrogen concentrations and loads in the Huaihe River Basin in relation to policies on pollution source control. *Sci. Total Environ.* **2018**, *642*, 1386–1395. [CrossRef]
36. Liu, G.; Li, L.; Song, K.; Li, Y.; Lyu, H.; Wen, Z.; Fang, C.; Bi, S.; Sun, X.; Wang, Z.; et al. An OLCI-based algorithm for semi-empirically partitioning absorption coefficient and estimating chlorophyll a concentration in various turbid case-2 waters. *Remote Sens. Environ.* **2020**, *239*, 111648. [CrossRef]
37. Xu, Y.; Feng, L.; Hou, X.; Wang, J.; Tang, J. Four-decade dynamics of the water color in 61 large lakes on the Yangtze Plain and the impacts of reclaimed aquaculture zones. *Sci. Total Environ.* **2021**, *781*, 146688. [CrossRef]
38. Zeng, S.; Du, C.; Li, Y.; Lyu, H.; Dong, X.; Lei, S.; Li, J.; Wang, H. Monitoring the particulate phosphorus concentration of inland waters on the Yangtze Plain and understanding its relationship with driving factors based on OLCI data. *Sci. Total Environ.* **2022**, *809*, 151992. [CrossRef]
39. Feng, L.; Hou, X.; Zheng, Y. Monitoring and understanding the water transparency changes of fifty large lakes on the Yangtze Plain based on long-term MODIS observations. *Remote Sens. Environ.* **2019**, *221*, 675–686. [CrossRef]
40. Liu, D.; Du, Y.; Yu, S.; Luo, J.; Duan, H. Human activities determine quantity and composition of dissolved organic matter in lakes along the Yangtze River. *Water Res.* **2020**, *168*, 115132. [CrossRef]
41. Ding, W.; Shi, G.; Zha, H.; Miao, H.; Lu, M.; Jin, J. Ecological impacts and supply demand evolution of the Yangtze to Huaihe water transfer project in Anhui section. *Sci. Rep.* **2024**, *14*, 20311. [CrossRef]
42. Mueller, J.L.; Fargion, G.S.; McClain, C.R. (Eds.) *Ocean Optics Protocols for Satellite Ocean Color Sensor Validation Revision 4 Volume III Radiometric Measurements and Data Analysis Protocols*; NASA/TM-2003-21621/Rev-Vol III; NASA Goddard Space Flight Center: Greenbelt, MD, USA, 2003.
43. Mobley, C.D. Estimation of the remote-sensing reflectance from above-surface measurements. *Appl. Opt.* **1999**, *38*, 7442–7455. [CrossRef]
44. Fang, C.; Song, C.; Wang, X.; Wang, Q.; Tao, H.; Wang, X.; Ma, Y.; Song, K. A novel total phosphorus concentration retrieval method based on two-line classification in lakes and reservoirs across China. *Sci. Total Environ.* **2024**, *906*, 167522. [CrossRef]
45. Li, J.; Zheng, Z.; Li, Y.; Lyu, H.; Ren, J.; Cai, X.; Du, C.; Chen, N.; Liu, G.; Lei, S.; et al. A hybrid algorithm for estimating total nitrogen from a large eutrophic plateau lake using Orbita hyperspectral (OHS) satellite imagery. *Int. J. Appl. Earth Obs. Geoinf.* **2024**, *131*, 103971. [CrossRef]
46. Li, J.; Li, Y.; Dong, X.; Wang, H.; Cai, X.; Zhu, Y.; Lyu, H.; Zeng, S.; Bi, S.; Wang, G. Contributions of meteorology and nutrient to the surface cyanobacterial blooms at different timescales in the shallow eutrophic Lake Taihu. *Sci. Total Environ.* **2023**, *894*, 165064. [CrossRef]

47. Zeng, S.; Qin, Z.; Ruan, B.; Lei, S.; Yang, J.; Song, W.; Sun, Q. Long-term dynamics and drivers of particulate phosphorus concentration in eutrophic lake Chaohu, China. *Environ. Res.* **2023**, *221*, 115219. [CrossRef]
48. Sun, Q.; Luo, W.; Dong, X.; Lei, S.; Mu, M.; Zeng, S. Landsat observations of total suspended solids concentrations in the Pearl River Estuary, China, over the past 36 years. *Environ. Res.* **2024**, *249*, 118461. [CrossRef]
49. Zeng, S.; Lei, S.; Qin, Z.; Song, W.; Sun, Q. Long-term remote observations of particulate organic phosphorus concentration in eutrophic Lake Taihu based on a novel algorithm. *Chemosphere* **2023**, *332*, 138836. [CrossRef]
50. Cai, X.; Lei, S.; Li, Y.; Li, J.; Xu, J.; Lyu, H.; Li, J.; Dong, X.; Wang, G.; Zeng, S. Humification levels of dissolved organic matter in the eastern plain lakes of China based on long-term satellite observations. *Water Res.* **2024**, *250*, 120991. [CrossRef]
51. Lee, Z.; Carder, K.L.; Hawes, S.K.; Steward, R.G.; Davis, C.O. Model for the Interpretation of Hyperspectral Remote-sensing Reflectance. *Appl. Opt.* **1994**, *33*, 5721–5732. [CrossRef]
52. Alexander, D.L.J.; Tropsha, A.; Winkler, D.A. Beware of R2: Simple, Unambiguous Assessment of the Prediction Accuracy of QSAR and QSPR Models. *J. Chem. Inf. Model.* **2015**, *55*, 1316–1322. [CrossRef]
53. Duan, H.; Ma, R.; Zhang, Y.; Loiselle, S.A. Variability of particulate organic carbon in inland waters observed from MODIS Aqua imagery. *Environ. Res. Lett.* **2014**, *9*, 084011. [CrossRef]
54. Jiang, D.; Matsushita, B.; Pahlevan, N.; Gurlin, D.; Fichot, C.G.; Harringmeyer, J.; Sent, G.; Brito, A.C.; Brotas, V.; Werther, M.; et al. Estimating the concentration of total suspended solids in inland and coastal waters from Sentinel-2 MSI: A semi-analytical approach. *ISPRS J. Photogramm. Remote Sens.* **2023**, *204*, 362–377. [CrossRef]
55. Xin, Y.; Luo, J.; Xu, Y.; Sun, Z.; Qi, T.; Shen, M.; Qiu, Y.; Xiao, Q.; Huang, L.; Zhao, J.; et al. SSAVI-GMM: An Automatic Algorithm for Mapping Submerged Aquatic Vegetation in Shallow Lakes Using Sentinel-1 SAR and Sentinel-2 MSI Data. *IEEE Trans. Geosci. Remote Sens.* **2024**, *62*, 1–10. [CrossRef]
56. Pitarch, J.; Vanhellemont, Q. The QAA-RGB: A universal three-band absorption and backscattering retrieval algorithm for high resolution satellite sensors. Development and implementation in ACOLITE. *Remote Sens. Environ.* **2021**, *265*, 112667. [CrossRef]
57. Vanhellemont, Q.; Ruddick, K. Atmospheric correction of Sentinel-3/OLCI data for mapping of suspended particulate matter and chlorophyll-a concentration in Belgian turbid coastal waters. *Remote Sens. Environ.* **2021**, *256*, 112284. [CrossRef]
58. Zhang, G.; Yao, T.; Chen, W.; Zheng, G.; Shum, C.K.; Yang, K.; Piao, S.; Sheng, Y.; Yi, S.; Li, J.; et al. Regional differences of lake evolution across China during 1960s–2015 and its natural and anthropogenic causes. *Remote Sens. Environ.* **2019**, *221*, 386–404. [CrossRef]
59. Prairie, Y.T. Evaluating the predictive power of regression models. *Can. J. Fish. Aquat. Sci.* **1996**, *53*, 490–492. [CrossRef]
60. Feng, C.; Xing, J.; Yuan, H.; Song, J.; Li, X.; Zhan, T.; Ma, J. Organic carbon in wet deposition of an urbanized coastal bay, North China: Flux, sources and biogeochemical implications. *Mar. Pollut. Bull.* **2024**, *201*, 116158. [CrossRef]
61. Yin, J.; Hu, W.; Chen, A.; Li, T.; Zhang, W. Human-caused increases in organic carbon burial in plateau lakes: The response to warming effect. *Sci. Total Environ.* **2024**, *937*, 173556. [CrossRef]
62. Li, J.; Wu, Y.; Peng, D.; Chen, M.; Peng, L.; Middleton, B.A.; Lei, T. Spatial Differences in Soil Nutrients Along a Hydrographic Gradient on Floodplains in Dongting Lake. *Water* **2024**, *16*, 3674. [CrossRef]
63. Abbass, K.; Qasim, M.Z.; Song, H.; Murshed, M.; Mahmood, H.; Younis, I. A review of the global climate change impacts, adaptation, and sustainable mitigation measures. *Environ. Sci. Pollut. Res. Int.* **2022**, *29*, 42539–42559. [CrossRef]
64. Behrenfeld, M.J.; Boss, E.S. Student's tutorial on bloom hypotheses in the context of phytoplankton annual cycles. *Glob. Change Biol.* **2018**, *24*, 55–77. [CrossRef]
65. Bellacicco, M.; Pitarch, J.; Organelli, E.; Martinez-Vicente, V.; Volpe, G.; Marullo, S. Improving the Retrieval of Carbon-Based Phytoplankton Biomass from Satellite Ocean Colour Observations. *Remote Sens.* **2020**, *12*, 3640. [CrossRef]
66. Kraal, P.; Burton, E.D.; Rose, A.L.; Kocar, B.D.; Lockhart, R.S.; Grice, K.; Bush, R.T.; Tan, E.; Webb, S.M. Sedimentary iron–phosphorus cycling under contrasting redox conditions in a eutrophic estuary. *Chem. Geol.* **2015**, *392*, 19–31. [CrossRef]
67. Marchand, J.; Schoefs, B. Editorial: Aquatic photosynthetic organisms under global change. *Front. Plant Sci.* **2024**, *15*, 1539716. [CrossRef]
68. Herbert, E.R.; Schubauer-Berigan, J.P.; Craft, C.B. Effects of 10 yr of nitrogen and phosphorus fertilization on carbon and nutrient cycling in a tidal freshwater marsh. *Limnol. Oceanogr.* **2020**, *65*, 1669–1687. [CrossRef]
69. Basu, S.; Mackey, K. Phytoplankton as Key Mediators of the Biological Carbon Pump: Their Responses to a Changing Climate. *Sustainability* **2018**, *10*, 869. [CrossRef]
70. Martiny, A.C.; Hagstrom, G.I.; DeVries, T.; Letscher, R.T.; Britten, G.L.; Garcia, C.A.; Galbraith, E.; Karl, D.; Levin, S.A.; Lomas, M.W.; et al. Marine phytoplankton resilience may moderate oligotrophic ecosystem responses and biogeochemical feedbacks to climate change. *Limnol. Oceanogr.* **2022**, *67*, S378–S389. [CrossRef]
71. Verspagen, X.J.J.M.H. Phenotypic plasticity of carbon fixation stimulatescyanobacterial blooms at elevated CO2. *Sci. Adv.* **2020**, *6*, eaax2926. [CrossRef]
72. Li, C.; Wang, Y.; Yi, Y.; Wang, X.; Augusto Guimarães Santos, C.; Liu, Q. A review of reservoir carbon Cycling: Key Processes, influencing factors and research methods. *Ecol. Indic.* **2024**, *166*, 112511. [CrossRef]

73. Yi, Y.; Li, S.L.; Zhong, J.; Wang, W.; Chen, S.; Bao, H.; He, D. The influence of the deep subtropical reservoir on the karstic riverine carbon cycle and its regulatory factors: Insights from the seasonal and hydrological changes. *Water Res*. **2022**, *226*, 119267. [CrossRef]
74. Baumas, C.; Bizic, M. A focus on different types of organic matter particles and their significance in the open ocean carbon cycle. *Prog*. *Oceanogr*. **2024**, *224*, 103233. [CrossRef]
75. Yue, Y.; Cai, L.; Tang, Y.; Zhang, Y.; Yang, M.; Wang, F. Vertical Distribution of Bacterial Community in Water Columns of Reservoirs With Different Trophic Conditions During Thermal Stratification. *Front*. *Environ*. *Sci*. **2021**, *9*, 632089. [CrossRef]
76. Qin, B.; Zhu, G.; Gao, G.; Zhang, Y.; Li, W.; Paerl, H.W.; Carmichael, W.W. A drinking water crisis in Lake Taihu, China: Linkage to climatic variability and lake management. *Environ*. *Manag*. **2010**, *45*, 105–112. [CrossRef]
77. Morales-Williams, A.M.; Wanamaker, A.D.; Williams, C.J.; Downing, J.A. Eutrophication Drives Extreme Seasonal CO2 Flux in Lake Ecosystems. *Ecosystems* **2020**, *24*, 434–450. [CrossRef]
78. Hu, M.; Ma, R.; Xiong, J.; Wang, M.; Cao, Z.; Xue, K. Eutrophication state in the Eastern China based on Landsat 35-year observations. *Remote Sens*. *Environ*. **2022**, *277*, 113057. [CrossRef]
79. Grbic, J.; Helm, P.; Athey, S.; Rochman, C.M. Microplastics entering northwestern Lake Ontario are diverse and linked to urban sources. *Water Res*. **2020**, *174*, 115623. [CrossRef]

Disclaimer/Publisher's Note: The statements, opinions and data contained in all publications are solely those of the individual author(s) and contributor(s) and not of MDPI and/or the editor(s). MDPI and/or the editor(s) disclaim responsibility for any injury to people or property resulting from any ideas, methods, instructions or products referred to in the content.